The Astrophysical Journal, 876:129 (9pp), 2019 May 10 https://doi.org/10.3847/1538-4357/ab18aa

High-resolution Observation of Moving Magnetic Features

Qin Li[1], Na Deng[1,2], Ju Jing[1,2], Chang Liu[1,2], and Haimin Wang[1,2]
[1] Space Weather Research Laboratory, New Jersey Institute of Technology, University Heights, Newark, NJ 07102-1982, USA; ql47@njit.edu
[2] Big Bear Solar Observatory, New Jersey Institute of Technology, Big Bear City, CA 92314-9672, USA
Received 2018 September 20; revised 2019 April 4; accepted 2019 April 9; published 2019 May 13

Abstract

Moving magnetic features (MMFs) are small magnetic elements moving almost radially away from sunspots toward the boundary of moat regions. They are mostly seen during the decay phase of a sunspot. Here we present a high-resolution observation of MMFs around a sunspot in NOAA AR 12565 on 2016 July 14 using the the 1.6 m Goode Solar Telescope (GST) at Big Bear Solar Observatory. The spectropolarimetric measurements of photospheric magnetic field are obtained from GST's newly commissioned Near Infra-Red Imaging Spectropolarimeter at the Fe I 1.56 μm line. The statistical study of physical properties of identified fine-scale MMFs (i.e., size, lifetime, inclination, horizontal velocity, and flux) is presented. The origin of the minority polarity flux in the sunspot is determined. Same as the majority polarity flux, the minority polarity flux can originate from mid-penumbra with highly inclined fields. The role of MMFs in both polarities in the flux evolution of the sunspot is speculated, as they can both contribute to the sunspot evolution.

Key words: Sun: activity – Sun: magnetic fields – Sun: photosphere

Supporting material: animations

1. Introduction

Moving magnetic features (MMFs) are small dynamic magnetic features moving from sunspots toward the boundary of the moat (an annular region surrounding the sunspot; Hagenaar et al. 2012). They were first found by Sheeley (1969), and then named and summarized by Harvey & Harvey (1973). MMFs are believed to be the intersection of magnetic flux tubes with the solar photosphere, and are often explained with the "sea-serpent" magnetic structure near the solar surface.

Previous studies have shown two types of MMFs: unipolar MMFs with the same/opposite polarity to the parent spot (Type II/Type III) and bipolar pairs of MMFs (Type I). Each type has a different sketch: unipolar MMFs are considered as the movement of single magnetic elements, while bipolar MMFs are the manifestation of Ω-shaped or U-shaped loops traveling along penumbral filaments (Zhang et al. 2003; Criscuoli et al. 2012). Type II MMFs formed as a result of the detached penumbral spines, and Type III MMFs are the results of intersections of the submerged penumbral flux (Thomas et al. 2002). They are modeled as manifestations of shocks and solitons propagating along the penumbral filaments (Ryutova & Hagenaar 2007). Their horizontal velocities are usually $\leqslant 1\ \mathrm{km\ s^{-1}}$ (Zhang et al. 2007; Criscuoli et al. 2012; Hagenaar et al. 2012). Bipolar MMFs may participate in the formation of a moat region, while unipolar MMFs are believed to be associated with chromospheric jets and microflares (Ryutova & Hagenaar 2007). Dynamic unipolar MMFs can interact with the opposite unipolar network magnetic features (NMFs) and cause cancellation and sequential solar jets (Yang et al. 2013; Chen et al. 2015). Compared to unipolar MMFs, bipolar ones have additional orientational parameters with respect to the sunspot. The boundary between unipolar and bipolar pairs are usually unclear. They can be mistaken for the other due to an improper threshold of chosen separation and unbalanced magnetic flux, especially when the opposite polarity feature is close to the sunspot, around which ambient flux is strong (Lee 1992).

In more recent observations, MMFs are found to originate from the mid-penumbra (Sainz Dalda & Bellot Rubio 2008). The magnetic features are intersections of horizontal fields extended from the penumbra with the photospheric surface in highly inclined fields (Kubo et al. 2003). The inclination of MMFs tends to be more and more vertical with MMF propagation due to the interaction with the magnetic canopy (Kaithakkal et al. 2017). Zhang et al. (2003) demonstrated the geometry and motion of MMFs between the main spot and the smaller opposite polarity spot, yet with an open question on whether MMF clustering depends on details of the magnetic and velocity fields.

MMFs can be related to the decay of sunspots (Harvey & Harvey 1973). As Meyer et al. (1974) suggested, the growth and decay of sunspots can be related to supergranular convection, and corresponding photospheric fields outside sunspots are concentrated into knots in a comparable size as that of granulation. Small flux tubes are transported away by the large-scale supergranulation from a sunspot, which are seen as MMFs in the moat. Martínez Pillet (2002) estimated that the rate of flux transport by appearance of Type II MMFs is 3–8 times larger than the flux decay rate of the sunspot. Kubo et al. (2003) agreed that Type II MMFs are responsible for the disintegration of the sunspot because the number of Type II MMFs is much larger than Type III MMFs. One reason for this conclusion is due to the lack of high spatial resolution vector magnetograms; the detection of Type III MMFs is influenced by strong ambient magnetic flux.

In this paper, photospheric vector magnetograms are obtained from the 1.6 m Goode Solar Telescope (GST; Cao et al. 2010; Goode et al. 2010) at Big Bear Solar Observatory (BBSO). The bipolar MMFs around a stable sunspot can be identified unambiguously. We studied the physical properties of all MMFs and their role in the sunspot flux evolution.

2. Observation and Data Description

The main data source is the vector magnetograms from the Near InfraRed Imaging Spectropolarimeter (NIRIS) of GST

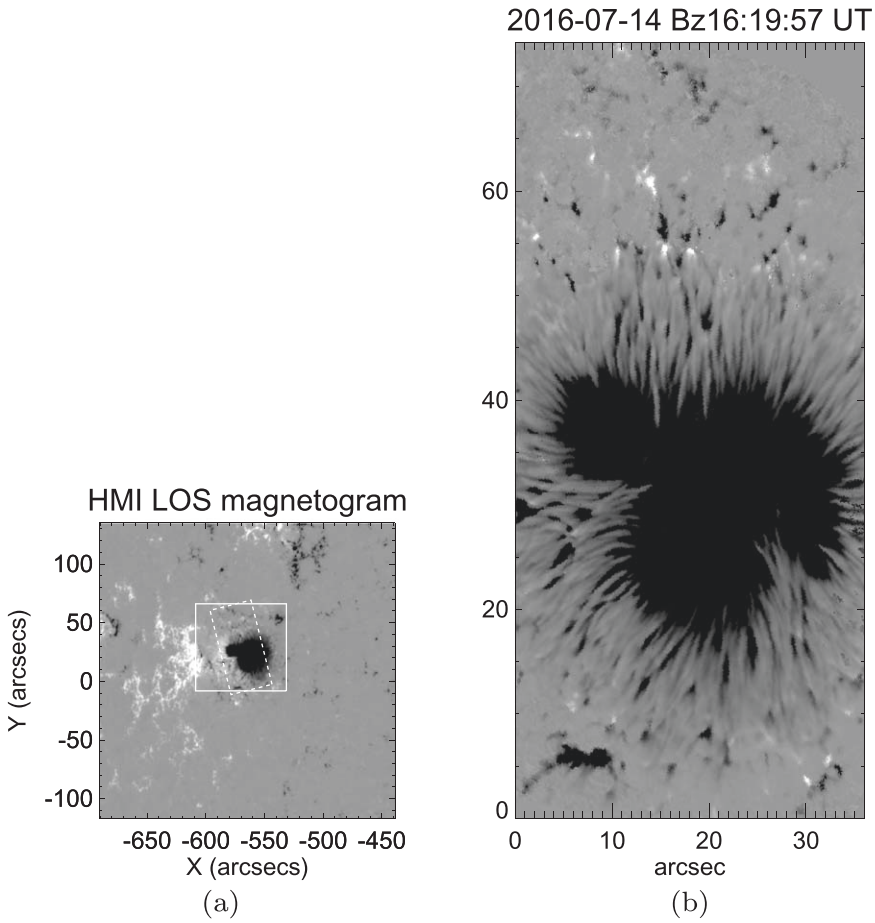

Figure 1. (a) Location of the sunspot in HMI LOS magnetogram. The solid box shows the original FOV of the NIRIS data, and the dashed box shows the region of data under study. (b) Vertical field of NIRIS data at 16:19:57 UT. An animation of NIRIS high-resolution observations is available online. The NIRIS animation runs from 16:19:57 UT to 22:53:42 UT.

(An animation of this figure is available.)

(Cao et al. 2012). GST is operated with a 308 element high-order AO system (Goode et al. 2010). In the visible wavelengths, the data acquired at GST achieve a spatial resolution around 0.″05 after using 100 frames for speckle reconstruction. The cadence of the data is 15 s. NIRIS was upgraded from the first-generation near-infrared imaging spectropolarimeter of BBSO. It offers unprecedented high-resolution spectroscopic and polarimetric imaging data of the solar atmosphere from the deepest photosphere through the base of the corona. NIRIS covers a broad spectral range from 1.0 to 1.7 μm, with particular attention to two main spectral lines: the Fe I 1565 nm line, which probes the magnetic field in the deepest photosphere, and the He I 1083 nm line, which is useful for mapping the vector field at the base of the corona (Cao et al. 2012). The sunspot under investigation was approximately located in the heliocentric coordinate (4″, −1″) on 2016 July 14, 16:19 UT. The cosine of the heliocentric angle is about 0.87 at that time. The data during our observation period (16:19 UT–22:53 UT) were used to conduct the study. In the observation, the field of view (FOV) of NIRIS covered the sunspot and the partial moat region from the outer penumbra of AR 12565, as illustrated in Figure 1. Polarimetric measurements of Stokes *I, Q, U, V* profiles ran at a 10 s cadence. Images were corrected for dark current, flat field, interference fringe, and polarization crosstalk. The diffraction-limited spatial resolution of vector magnetograms reached 0.″24. The polarization noise was $\sim 10^{-3}$ I_c, where I_c is the continuum intensity (Cao et al. 2012). The Stokes vectors were inverted using the Milne–Eddington inversion method (Orozco Suárez et al. 2010), which solves the polarized radiative transfer equation and fits the Stokes line profiles. The inversion procedure returned parameters including magnetic field, inclination, azimuth angle, and Doppler center shift. The inverted data then underwent the 180° azimuth ambiguity correction by using the minimum-energy method (Leka et al. 2009), which simultaneously minimizes the electric current density and the field divergence. Because the azimuth ambiguity is not fully resolved in other regions, we only study a central subregion of data (as denoted by the dashed box in Figure 1) within the original FOV (as denoted by the solid box in Figure 1) mainly covering the sunspot and northwestern region. The noise of NIRIS varied with locations in the FOV. A denoise algorithm was implemented to assign a denoise mask. In the surrounding $5 \times 5 \times 5$ pixel^3 cube, isolated pixels as singularities were detected and smoothed out by the linear least-squares interpolation.

To validate the NIRIS data, we compared the $B_{\rm los}$, $B_{\rm transvers}$, and azimuth obtained with NIRIS and the *Solar Dynamics*

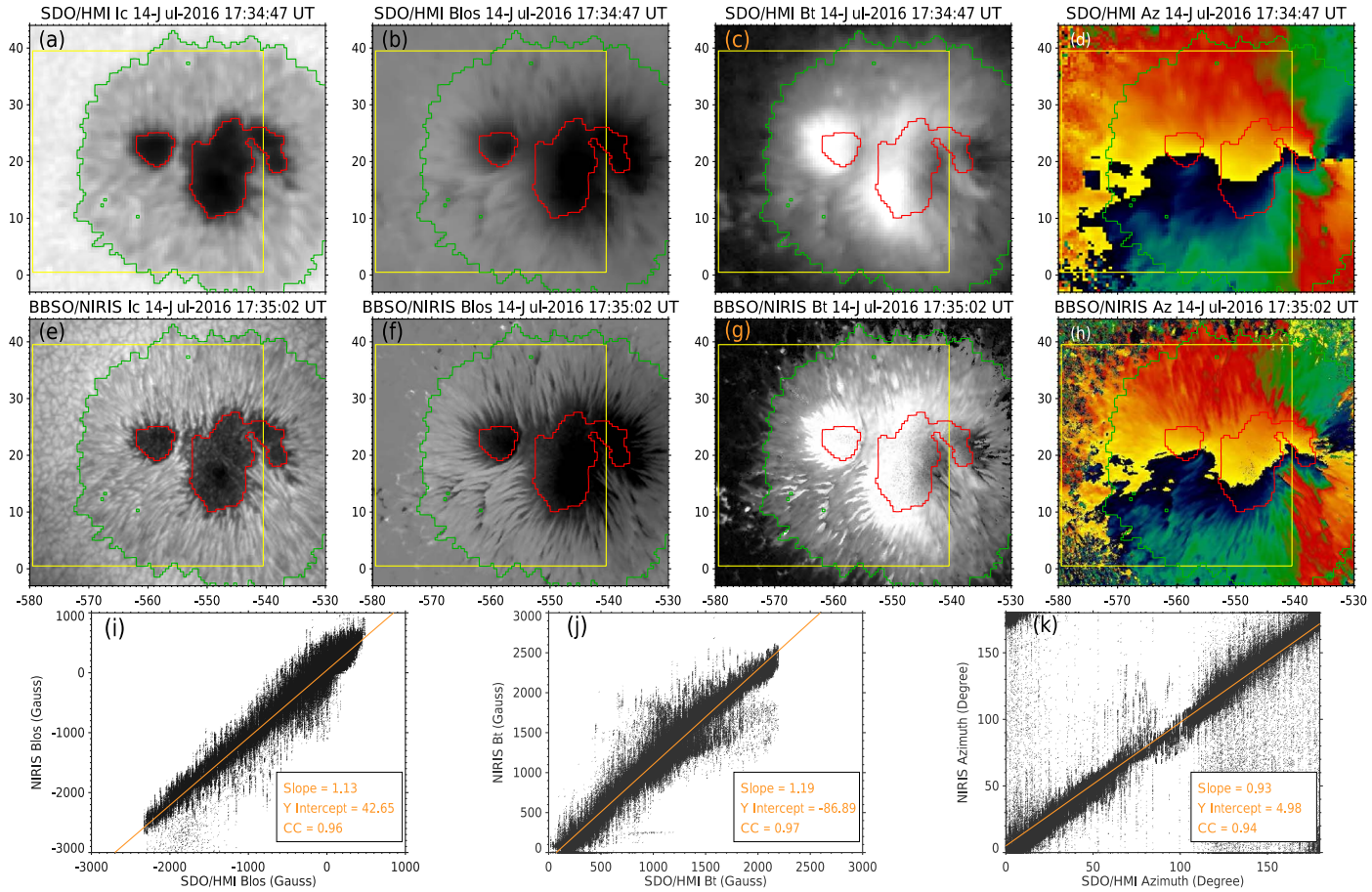

Figure 2. Comparisons of continuum intensity, $B_{\rm los}$, $B_{\rm transvers}$, and azimuth between HMI and NIRIS vector magnetograms. Top panel: HMI data. Middle panel: NIRIS data. Bottom panel: correlation results between HMI and NIRIS data. HMI data were rescaled for comparison with NIRIS data. The yellow box shows the region used for the comparison. The red and green contours highlight locations of umbra and penumbra, respectively. The red lines in the bottom panels show the linear fitting of comparisons.

Observatory (*SDO*) Helioseismic and Magnetic Imager (HMI; Schou et al. 2012) vector magnetograms. Visual inspection of images in Figure 2 shows that magnetograms derived from *SDO*/HMI and NIRIS data show a good agreement. This is also confirmed through the calculation of the Pearson correlation coefficient. The NIRIS data products measured at 17:35 UT were compared to the cotemporal *SDO*/HMI data products over a common area marked by the yellow box in Figure 2. 10^5 pixel pairs were used to obtain the regression relationship between NIRIS and *SDO*/HMI data products. The linear regression coefficients of $B_{\rm los}$, $B_{\rm transvers}$, and azimuth between *SDO*/HMI and NIRIS magnetograms are close to 1.0, while the Pearson correlation coefficients are larger than 0.94, indicating a strong correlation between the pair of data products.

3. Identification and Tracking of MMFs

Type II and III MMFs around the sunspot are identified by the Yet Another Feature Tracking Algorithm (YAFTA; Welsch & Longcope 2003). Type I MMFs are classified as Type II and III MMFs, and will be discussed in Section 4.3. The intensity and size threshold levels are set to be $\pm$100 Gauss and 0.07 $\rm Mm^2$. As suggested by DeForest et al. (2007), feature identification uses a clumping algorithm to keep tracking flux clusters. Differences among the identification methods, such as clumping, the downhill, and curvature have been discussed in DeForest et al. (2007). The clumping algorithm may merge MMFs in the same polarity, but it does not affect the separation of Type II and III MMFs. The code returns the spatial location of features, each of which is masked with a specific identification number. Values of all relevant parameters such as flux density, inclination, and azimuthal angle can be obtained. MMFs are tracked over consecutive B_z maps based on the estimated centroid positions. Considering the differences of physical properties between MMFs and NMFs, they are distinguished based on the following facts: (1) MMFs tend to move outward away from the sunspot, while NMFs drift inward. (2) The velocity of NMFs is less than 0.5 $\rm km\,s^{-1}$. (3) MMFs are inside the moat, while NMFs are outside the moat. Some large network patches within the moat are excluded from MMFs manually. In total, 268 MMFs and 16 NMFs are found around the sunspot. There are 137 negative MMFs, 131 positive MMFs, 15 negative NMFs, and 1 positive NMF.

4. Results

The tracking results of all magnetic features by using YAFTA over 6.5 hr of observation in B_z can be seen in Figure 3(a). The original positions (roots of the arrows) and the

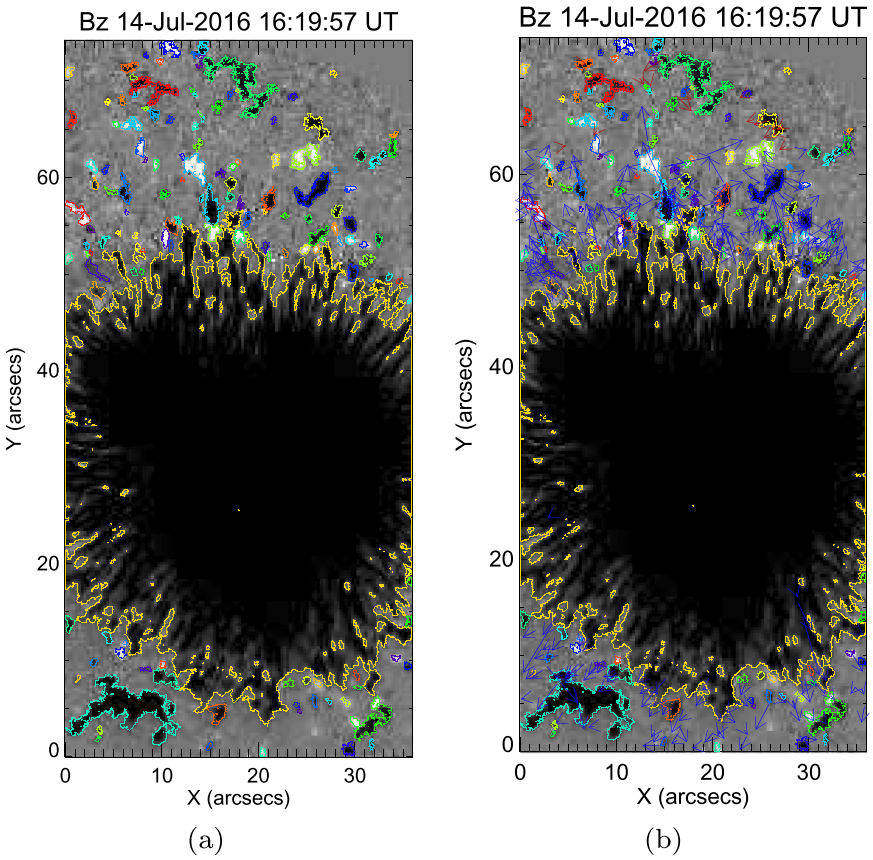

Figure 3. (a) All magnetic features identified and outlined in different color by YAFTA. (b) Moving trajectories of MMFs derived from the centroid position of each MMF in each frame. The blue arrows and red arrows represent the trajectories of MMFs and NMFs, respectively. An animation of the YAFTA result sequence is available online. The YAFTA animation runs from 16:19:57 UT to 22:53:42 UT; it does not include trajectory arrows.

(An animation of this figure is available.)

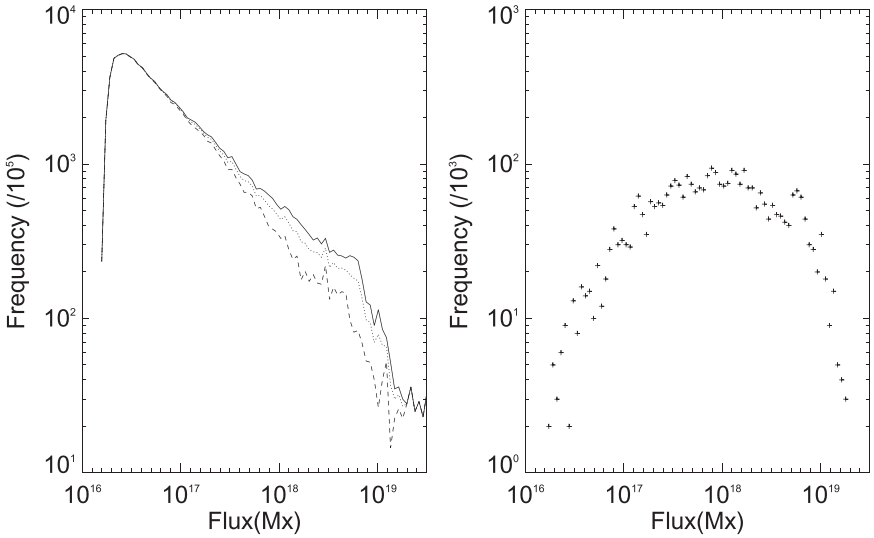

Figure 4. (a) Histogram of magnetic fluxes observed in NIRIS data. The top solid line represents the whole data set. The middle dotted line represents the data set without taking MMFs into account. The lower dashed line represents the data set with 2.5 times of the flux removed. (b) Histogram of MMFs identified by YAFTA.

moving direction of the centroid of MMFs over 6.5 hr are shown in Figure 3(b). MMFs are distributed mostly from the outer penumbra to the boundary of the moat region. NMFs are mostly rooted around the boundary of the moat region and slowly drift around.

The distribution of overall magnetic features excluding sunspot umbra and penumbra and isolated MMFs only are shown in Figure 4. In Figure 4(a), three lines from top to bottom represent overall magnetic features ($F_{\rm all}$), the magnetic features excluding MMFs ($F_{\rm all}$–$F_{\rm MMF}$), and the magnetic

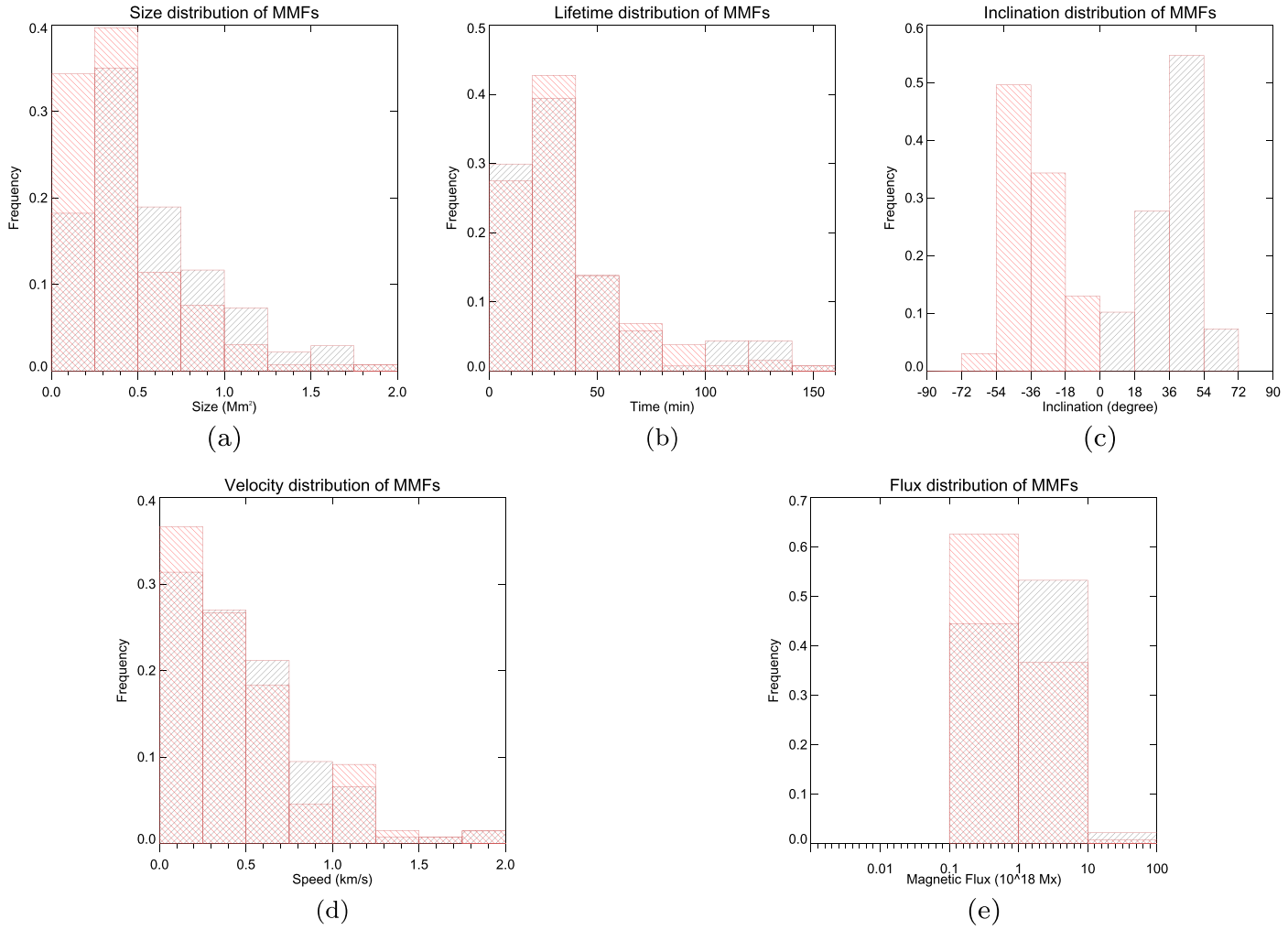

Figure 5. Histogram of the lifetime average of size (a), lifetime (b), inclination (c), $V_{\rm horizontal}$, (d) and flux density of MMFs (e). Red (black) plots represents Type II (III) MMFs.

features excluding 2.5 times MMFs ($F_{\rm all} - 2.5 \times F_{\rm MMF}$). The overall magnetic features have a tendency to yield power-law distribution. The low flux tail of the distribution falls off because fluxes below the threshold are ignored. The linear fitting line has a broken slope of 0.4 before 6×10^{18} Mx and 1.81 after 6×10^{18} Mx. This does not agree well with Parnell et al. (2009), which suggested a scale-free power-law distribution with slope of 1.85 for all surface magnetic features. After removal of MMFs (middle dotted line), the turning point at 6×10^{18} Mx becomes smoother. Multiplying the total flux of MMFs by a factor of 2.5 makes the slope to be 1.81 as shown in the bottom dashed line. This may hold true due to the lack of observations of the west and east sides of the sunspot. Unlike most of the surface magnetic features, the characteristic flux of MMFs is $\sim 10^{18}$ Mx. Considering the Gaussian form of the MMF flux distribution, lowering the threshold to include more flux of MMFs will not change the result, as it will only expand the peripheral flux while the center part of the flux density still remains ~1500 G. The difference between overall magnetic features and MMFs was first shown in the *Hinode*/SOT observation in 2007 by Hagenaar et al. (2012), in which the overall magnetic features yield a simple power-law distribution, while MMFs do not follow this distribution.

4.1. Physical Properties of MMFs

Distributions of MMFs' size, lifetime, inclination, velocity, and magnetic flux are shown in Figure 5. NMFs are removed from the data sets. For Type II and III MMFs, their sizes are all below 2.0 Mm^2 with a median of 0.4 Mm^2. They show very similar distribution, which may imply the balance of two polarities.

The mean lifetime of Type II and III MMFs is 43 min, comparable to the 1 hr found by Hagenaar & Shine (2005), but less than the 4 hr found by Zhang et al. (2003). Note that the clumping method is implemented to identify and track MMFs. Surface process, such as fragmentation, coalescence, and cancellation, which mostly happens at the boundary of the moat region, will create new feature masks.

Panel (c) shows the inclination of MMFs. The mean inclination of Type III MMFs is about $-57°$ and that of Type II MMFs is about 56°. A portion of MMFs can be highly inclined. As suggested by previous studies (Criscuoli et al. 2012; Kaithakkal et al. 2017), with an increasing distance from

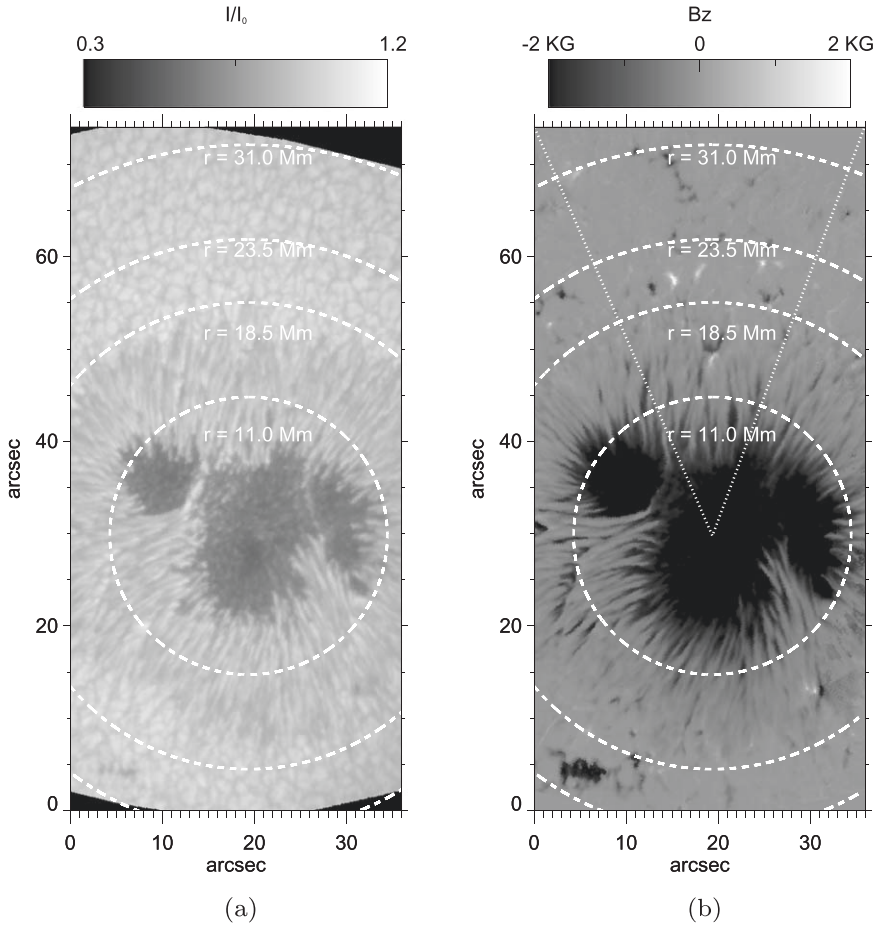

Figure 6. Snapshots of the sunspot at 19:12:44 UT. (a) Continuum intensity image, scaled between 30% and 120% of the intensity maximum of the quiet region. (b) Vertical magnetic field B_z, scaled between −2000 Gauss and +2000 Gauss. Four concentric arcs are drawn to show the distances from the sunspot center. Their radius is annotated in both panels. Dotted lines mark the area for the flux calculation in Figure 8.

the sunspot, magnetic fields of MMFs tend to be more vertical. This is shown clearly in Figure 7.

In panel (d), the horizontal velocity in MMFs ranges from 0.0 to 2.0 km s^{-1}. Mean velocity of MMFs is 0.5 km s^{-1}.

As shown in Figure 5(e), the total signed flux of MMFs ranges between $10^{17} \sim 10^{19}$ Mx, with an average value of 1.1×10^{18} Mx. This agrees well with an average flux of 3.6×10^{18} Mx deduced from MDI (Zhang et al. 2003), 2.5×10^{18} Mx also from MDI (Hagenaar & Shine 2005), but much larger than 1.16×10^{17} Mx deduced from SUNRISEII/IMaX around a pore (Kaithakkal et al. 2017). As suggested by Kaithakkal et al. (2017), the flux density of MMFs around a pore may be as small as 1000 G, whereas in our study most of them are around 1500 G. The flux density of a unipolar MMF may fluctuate randomly during its motion to the boundary of moat. Note that the lower limit of the magnetic strength of identified MMFs is 6.5×10^{16} Mx, which is sufficient to detect MMFs.

4.2. Variation of MMFs as a Function of Distance from Sunspot Center

In Figure 6, we show the NIRIS continuum intensity and vertical field around the sunspot from NIRIS data. East–west regions are cut off due to missing data when conducting the 180 disambiguity procedures. Four concentric circles marked in dashed lines have a radius $r = 11.0$, 18.5, 23.5, 31.0 Mm, corresponding to the boundary of umbra, outer penumbra, moat region, and FOV, respectively. Azimuthal and temporal averages of the intensity, inclination, $\mathrm{Flux_{signed}}/\mathrm{Flux_{unsigned}}$, and radial velocity as a function of distance from the center of the sunspot are shown in Figure 7.

In Figure 7(a), the azimuthally averaged inclination around the sunspot shows a magnetic dome structure, which can also be seen in the sunspot simulation study by Rempel (2012). Both positive and negative MMFs originate with a highly inclined field topology, and become more and more vertical along the way to the boundary of the moat at a rate of 7° Mm^{-1}. The origin of Type III MMFs can be intraspines in a penumbral uncombed structure, where a more horizontal magnetic component is present (Deng et al. 2010; Wang et al. 2012). Such a tendency for inclination angle to become more vertical was also confirmed by Criscuoli et al. (2012).

In Figure 7(b), both Type II and III MMFs show strong downflows, with a mean V_{los} of 0.7 and 1.5 km s^{-1}, respectively. The V_{los} values of the Type III MMFs are similar to previous results, e.g., 1.0 km s^{-1} reported by Criscuoli et al. (2012), but the direction of the flow is opposite. A strong upflow trend for Type III MMFs is presented by Criscuoli et al. (2012) and Kaithakkal et al. (2017).

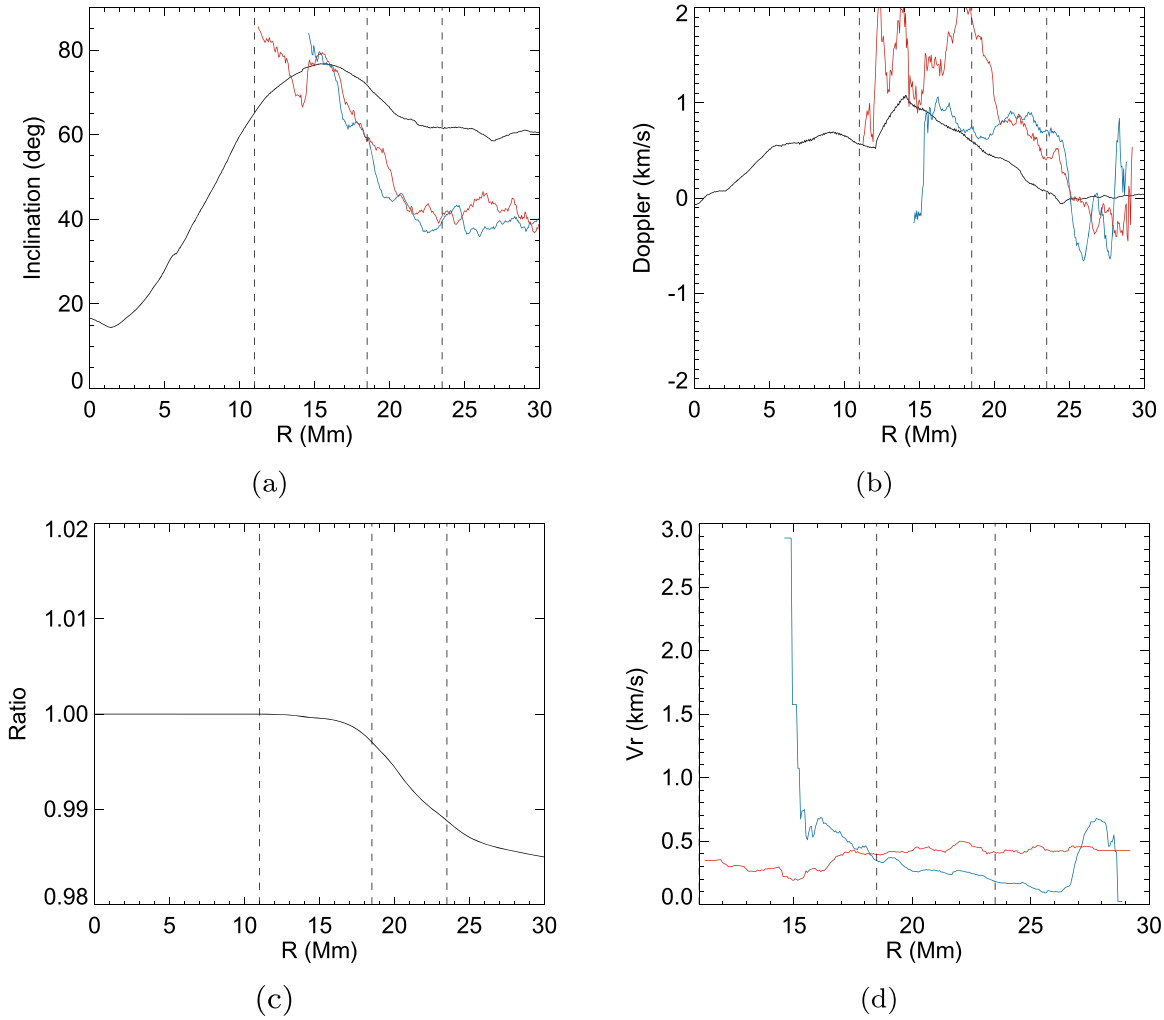

Figure 7. Azimuthally averaged quantities on photosphere. (a) Inclination. (b) Line-of-sight velocity. (c) Ratio of signed flux over unsigned flux. (d) Radial component of horizontal velocity. Black line represents the whole magnetogram, and blue (red) lines represent Type II (III) MMFs.

To determine the origin of Type III MMFs, we present the ratio of $\mathrm{Flux_{signed}}/\mathrm{Flux_{unsigned}}$ shown in Figure 7(c). Gradual polarity reversal of the magnetic flux can be found in mid-penumbra, at $r = 12$ Mm in this case, where the total signed flux becomes less than the total unsigned flux within the same circular region. Inverse polarity flux was also observed in *Hinode* for a larger positive polarity sunspot (Sainz Dalda & Bellot Rubio 2008). In a sunspot simulation modeled by Rempel (2012), inverse polarity flux occurs between 10 and 15 Mm away from the sunspot center for the optical depth from $\tau = 1$ to $\tau = 0.001$. Resolution may also lead to a shift of inverse polarity flux in ~2 Mm.

The azimuthally averaged velocity is shown in Figure 7(d). Radial components of horizontal velocity V_r of Type II MMFs begin with 3.0 km s^{-1}, which is highly affected by the evershed flow velocity. It decreases to 0.15 km s^{-1} at the boundary of the moat. The slope of linear regression for Type II MMFs is around −4.4 along with the penumbral evershed flow, −0.18 in the penumbra, and 0.03 in the moat. V_r of Type III MMFs keeps relatively stable. The bump at Mm = 27 is mainly due to the instability of the feature identification, as frequent cancellation occurs at the boundary of the moat.

4.3. Flux Transport of MMFs and Sunspot

The tempo-spatial evolution of the magnetic flux and flux transport rate is shown in Figure 8. The flux transport rate is calculated in an angle range of the $\theta = 25°$ region shown in Figure 6(b). The flux transport rate as a function of distance from the sunspot center (Kubo et al. 2008) is

$$F_v = \frac{\sum F(r) \cdot V_r(r)}{\pi(r_2^2 - r_1^2)} \cdot \frac{2\pi(r_1 + r_2)}{2} \cdot \frac{\pi}{\theta}.$$

Here, r_1 and r_2 are inner and outer annular radius, $\theta = 25°$.

From Figure 8(a), negative and positive MMFs show very strong serpent wave spatial distribution when they moved out from the sunspot. Dominant MMFs are about $\pm 2.0 \times 10^{19}$ Mx. Separation of their centroid increases from around 1.8 Mm to 3.0 Mm. In Figure 8(b), the dominant flux transport rate for Type II MMFs is $\sim -2.0 \times 10^{20}$ Mx h^{-1}, with a median flux rate $\sim -1.64 \times 10^{19}$ Mx h^{-1}. Type III MMFs have a similar value of dominant flux transport rate, but with a larger median flux rate $\sim 2.47 \times 10^{19}$ Mx h^{-1}. The flux transport rate of the Type II MMFs found in this study agrees well with that found by Kubo et al. (2003). However, Kubo et al. (2003) also find that the transport rate of the Type II MMFs is 50 times larger than that of the Type III MMFs, which is not the case in our study. Note that

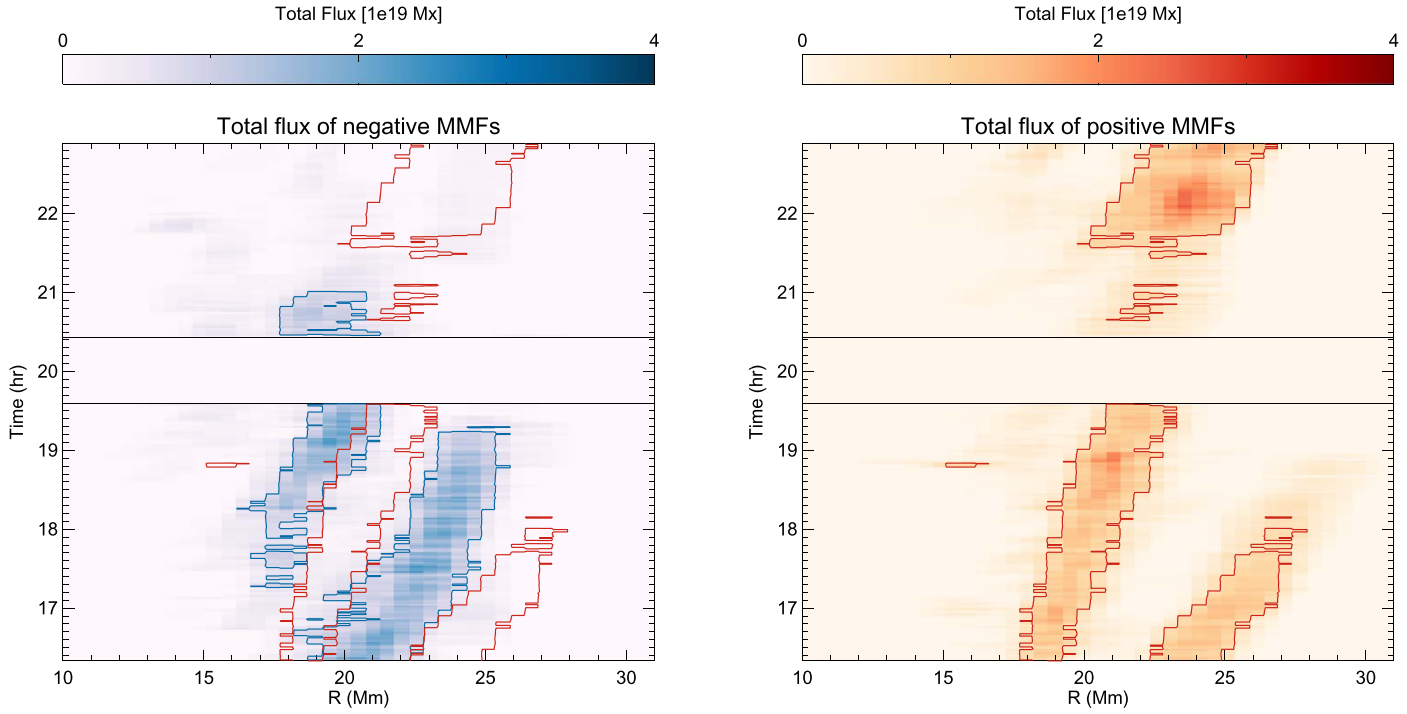

Figure 8. (a) Temporal and spatial evolution of the total flux of Type II (III) MMFs around the sunspot. Blue (red) contours represent the total flux of Type II (III) MMFs above 2.0×10^{19} Mx. (b) Temporal and spatial evolution of flux transport rate due to Type II (III) MMFs. Blue (red) contours represent the flux transport rate due to Type II (III) MMFs above $\sim 2.0 \times 10^{20}$ Mx·Hr^{-1}.

only the flux transport rate of the vertical MMFs is considered. The flux transport rate of the vertical MMFs should be more important than horizontal ones because horizontal MMFs sometimes correspond to the local fluctuation of the magnetic field (Kubo et al. 2003). Our sunspot is in a stable phase, with a flux evolution rate of vertical field $\sim 1.79 \times 10^{19}$ Mx h^{-1}. The median net flux transport of MMFs agrees well with the flux evolution of the sunspot.

5. Conclusion

The physical properties of Type II and III MMFs on subarcsecond size are studied. In previous studies, Type II and III MMFs are imbalanced, due to the limitation of observations (Kubo et al. 2003; Hagenaar et al. 2012). In our study, Type II and III MMFs have a similar distribution of size, lifetime, inclination, horizontal velocity, and balanced flux strength, which implies the same origin and symmetric properties of MMFs in both polarities.

The overall distribution of magnetic features confirms that the scale-free power-law distribution between 3.0×10^{16}–2.0×10^{19} Mx tends to hold after the removal of the MMFs. MMFs have a characteristic flux $\sim 10^{18}$ Mx, which does not follow the scale-free power-law distribution. It may imply a different mechanism upon the generation of MMFs compared to other global surface magnetic features.

Type III MMFs may originate from mid-penumbra, where the fields of penumbral filaments are the most inclined. Same as Type II MMFs, Type III MMFs are shredded from the extension of the penumbral filaments with highly inclined fields. With the distance from the sunspot, all MMFs tend to become more and more vertical as the result of the interaction with magnetic canopy, and the velocity of Type II MMFs decreases until reaching the boundary of the moat. Type III MMFs are associated with downflows instead of upflows, which is contrary to previous studies (Criscuoli et al. 2012; Kaithakkal et al. 2017). Though they show stronger line-of-sight velocity than Type II ones.

For all MMFs that originate from the mid-penumbra to the boundary of the moat, Type I MMFs dominate. Type II and III MMFs may carry a similar amount of the opposite flux. Resolvable separation of 2 Mm is needed to find out the bipolar structure near the outer penumbra. As Type III MMFs can be found in mid-penumbra, even at a shorter distance than Type II ones, they should also be accountable for sunspot flux evolution. In previous studies, only Type II MMFs are thought to be responsible for sunspot flux loss (Kubo et al. 2003), as Type III MMFs had seldom been found near the outer penumbra. The net flux transport rate for MMFs with both polarities is derived. The sunspot flux evolution rate is much smaller than the flux transport rate of the Type II MMFs, but is comparable with the net flux transport rate. Therefore, MMFs do not have to be associated with sunspot decay. The transition from balance to imbalance of the flux transport rate of Type II and III MMFs may be associated with sunspot decay.

We thank the BBSO team for the excellent data of this event. We also thank the Southwest Research Institute for the tracking code. The BBSO operation is supported by NJIT and US NSF AGS 1821294 grant. The GST operation is partly supported by the Korea Astronomy and Space Science Institute and Seoul National University, and by the strategic priority research program of CAS with grant No. XDB09000000. This work was supported by NASA grants NNX16AF72G, 80NSSC17K0016, 80NSSC18K0673, 80NSSC18K1705, and 80NSSC19K0257 and by NSF grants AGS 1408703 and 1821294.

ORCID iDs

Na Deng https://orcid.org/0000-0001-8179-812X
Ju Jing https://orcid.org/0000-0002-8179-3625
Chang Liu https://orcid.org/0000-0002-6178-7471
Haimin Wang https://orcid.org/0000-0002-5233-565X

References

Cao, W., Goode, P. R., Ahn, K., et al. 2012, in Magnetic Fields from the Photosphere to the Corona 463, Second ATST-EAST Meeting, ed. T. Rimmele et al. (San Francisco, CA: ASP), 291
Cao, W., Gorceix, N., Coulter, R., et al. 2010, AN, 331, 636
Chen, J., Su, J., Yin, Z., et al. 2015, ApJ, 815, 71
Criscuoli, S., Del Moro, D., Giannattasio, F., et al. 2012, A&A, 546, A26
DeForest, C. E., Hagenaar, H. J., Lamb, D. A., Parnell, C. E., & Welsch, B. T. 2007, ApJ, 666, 576
Deng, N., Prasad Choudhary, D., & Balasubramaniam, K. S. 2010, ApJ, 719, 385
Goode, P. R., Yurchyshyn, V., Cao, W., et al. 2010, ApJL, 714, L31
Hagenaar, H., Shine, R., Ryutova, M., et al. 2012, in Hinode-3: The III Hinode Science Meeting, ed. T. Sekii, T. Watanabe, & T. Sakurai (San Francisco, CA: ASP), 181
Hagenaar, H. J., & Shine, R. A. 2005, ApJ, 635, 659
Harvey, K., & Harvey, J. 1973, SoPh, 28, 61
Kaithakkal, A. J., Riethmüller, T. L., Solanki, S. K., et al. 2017, ApJS, 229, 13
Kubo, M., Lites, B. W., Shimizu, T., et al. 2008, ApJ, 686, 1447
Kubo, M., Shimizu, T., & Lites, B. W. 2003, ApJ, 595, 465
Lee, J. W. 1992, SoPh, 139, 267
Leka, K. D., Barnes, G., Crouch, A. D., et al. 2009, SoPh, 260, 83
Martínez Pillet, V. 2002, AN, 323, 342
Meyer, F., Schmidt, H. U., Wilson, P. R., & Weiss, N. O. 1974, MNRAS, 169, 35
Orozco Suárez, D., Bellot Rubio, L. R., & Del Toro Iniesta, J. C. 2010, A&A, 518, A3
Parnell, C. E., DeForest, C. E., Hagenaar, H. J., et al. 2009, ApJ, 698, 75
Rempel, M. 2012, ApJ, 750, 62
Ryutova, M., & Hagenaar, H. 2007, SoPh, 246, 281
Sainz Dalda, A., & Bellot Rubio, L. R. 2008, A&A, 481, L21
Schou, J., Scherrer, P. H., Bush, R. I., et al. 2012, SoPh, 275, 229
Sheeley, N. R., Jr. 1969, SoPh, 9, 347
Thomas, J. H., Weiss, N. O., Tobias, S. M., & Brummell, N. H. 2002, AN, 323, 383
Wang, H., Deng, N., & Liu, C. 2012, ApJ, 748, 76
Welsch, B. T., & Longcope, D. W. 2003, ApJ, 588, 620
Yang, L., He, J., Peter, H., et al. 2013, ApJ, 777, 16
Zhang, J., Solanki, S. K., & Wang, J. 2003, A&A, 399, 755
Zhang, J., Solanki, S. K., Woch, J., et al. 2007, A&A, 471, 1035